ACS APPLIED MATERIALS & INTERFACES

www.acsami.org

Research Article

Integrating Multi-Level Micro/Nanostructures to Synergistically Regulate Contact Behavior and Mechanical Deformation for Broad-Range High-Sensitivity Pressure Sensors

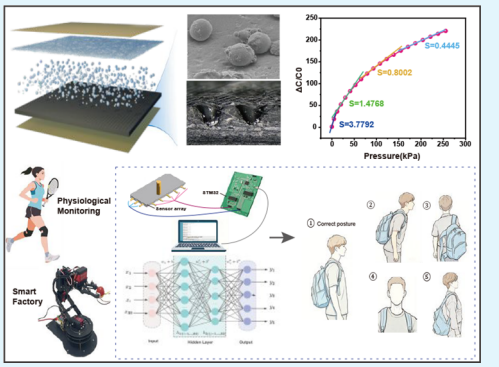
Jiaqi Xu,‡ Lanxin Ji,‡ Peizhi Jiang,‡ Jiawei Wu, Yun-Woo Lee, Junseong Ahn, Bingjun Yu, Caijiang Lu, and Zhi-Jun Zhao*

Cite This: *ACS Appl. Mater. Interfaces* 2026, 18, 43404−43417

Read Online

ACCESS | Metrics & More | Article Recommendations | Supporting Information

ABSTRACT: Flexible capacitive pressure sensors hold tremendous promise for human health monitoring, human-machine interfaces, and wearable electronics due to their excellent conformability and high sensitivity. Nevertheless, breaking the inherent trade-off between high sensitivity and a broad detection range remains a challenge. Herein, we rationally design a hierarchical micro/nanostructured capacitive pressure sensor. This architecture strategically integrates a conical microcavity layer to optimize mechanical compressibility, a SiO_2 micro/nanosphere layer to regulate interfacial contact behavior, and an electrospun nanofiber network to reinforce structural robustness, working synergistically to achieve superior sensing performance. Empowered by these synergistic components, the sensor exhibits an outstanding comprehensive performance, achieving a high sensitivity of 3.779 kPa^{-1}, a broad sensing range of up to 255 kPa, a rapid response time (48 ms), and remarkable mechanical durability (over 6000 cycles under a high pressure of 150 kPa). Consequently, the sensor demonstrates versatile capabilities across diverse scenarios, including continuous human physiological and kinematic monitoring, non-destructive fruit and vegetable sorting, high-resolution pressure array sensing, and a backpack-integrated posture assessment system. This work establishes a versatile hierarchical design paradigm for next-generation flexible capacitive sensors, paving the way for superior performance and real-world applications in intelligent perception systems.



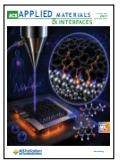
KEYWORDS: *capacitive pressure sensor, conical microcavity structure, SiO_2 micro-nano spheres, high sensitivity, deep learning*

1. INTRODUCTION

Flexible pressure sensors, which convert external mechanical pressure into dynamic electrical signals, have been extensively investigated for health monitoring,[1−3] human-machine interaction,[4−6] and wearable applications.[7,8] Among the diverse transduction mechanisms—including piezoresistive,[9,10] piezoelectric,[11−13] and triboelectric[14,15]—capacitive sensors[16−18] have attracted particular attention due to their structural simplicity, minimal power consumption, and high sensitivity. Despite these advantages, reconciling the inherent conflict between sensitivity and detection range remains a critical, unresolved challenge in current capacitive sensor research.

Fundamentally, flexible capacitive pressure sensors are typically built with a flexible dielectric layer between two electrodes. Their sensitivity mainly depends on the changes in plate distance and effective dielectric constant when external force is applied. Thus, a dielectric layer with high mechanical deformability and a large dielectric constant is key to better performance. To date, the mainstream strategies for optimizing the performance of capacitive pressure sensors fall into two categories: dielectric layer modification and electrode modification. There are two primary approaches for dielectric layer optimization: structuring the dielectric layer (e.g., pyramid,[19,20] micro-pillar,[21] or folded shapes[22,23]) or modifying the composite materials (e.g., using PDMS, PVDF, MWCNTs, silver nanowires, or graphene). Besides the dielectric layer, the material selection and structural design of electrodes also play a decisive role in sensor performance. Traditional rigid metal electrodes are prone to electrical failure under repeated bending and stretching. To address this issue, a variety of flexible conductive materials including ionic gel, carbon nanotubes and liquid metals have been developed for electrode fabrication,[24,25] which greatly improve the cycling stability of devices. In addition, the construction of microstructured electrodes and interdigital electrodes can effectively increase the effective contact area between

Received: May 10, 2026
Revised: July 15, 2026
Accepted: July 15, 2026
Published: July 27, 2026



Downloaded from pubs.acs.org/aamick/article-pdf/18/31/43404/6628714/am-2026-09373q.pdf by KOREA UNIV user on 23 September 2026

ACS Publications

© 2026 American Chemical Society

electrodes and the dielectric layer, and further enhance the response intensity of capacitive signals.[26,27] Despite these efforts, it is hard to balance sensitivity and detection range. Most existing studies have achieved breakthroughs in only a single performance metric and suffer from prominent limitations: certain studies have attained high sensitivity yet are confined to extremely low-pressure ranges, resulting in a narrow detection window. For example, Li et al.[28] introduced magnetically grown microneedle array as the dielectric layer for flexible capacitive pressure sensors. By precisely controlling the magnetic particle concentration and dynamic magnetic field strength, they achieved a high sensitivity of 4.11 kPa^{-1} within the pressure range of 0–1 kPa. Inspired by the structure of skin tissue, Zhang and co-workers[29] fabricated an embedded sensor composed of liquid metal microstructured electrode (LM-ME) array, which exhibited an outstanding sensitivity of 7.42 kPa^{-1}. Nevertheless, such high sensitivity was only attained in the low-pressure region of 0–0.1 kPa, accompanied by a restricted detection range (≤20 kPa). Conversely, sensors engineered for a broad measurement range typically necessitate stiffer structural designs to prevent premature collapse, which inevitably sacrifices low-pressure responsiveness. For instance, Zhong et al.[30] used a gradient dome structure to achieve a wide range of 0–200 kPa, but the sensitivity dropped to 0.214 kPa^{-1}. Overall, the synergistic optimization of high sensitivity, wide detection range, and long-term stability remains a core unresolved issue in the field of flexible capacitive pressure sensors.

To address this long-standing dilemma, herein, we propose a rationally designed capacitive pressure sensor featuring a robust hierarchical architecture. Specifically, the device integrates copper electrodes, a thermoplastic polyurethane (TPU) filament network, multi-size SiO_2 micro/nanospheres (30 μm and 200 nm), and a composite dielectric layer characterized by micro-conical cavities. To boost the inherent sensing capacity, multi-walled carbon nanotubes (MWCNTs) are uniformly dispersed within a polydimethylsiloxane (PDMS) matrix, effectively elevating the overall dielectric constant. Furthermore, the interfacial spin-coating of the multi-size SiO_2 spheres introduces abundant compressible air gaps and optimizes the interfacial contact mechanics between the dielectric layer and electrodes, significantly amplifying the sensing response. Meanwhile, the incorporation of the TPU filament layer mechanically reinforces the system, ensuring exceptional cyclic stability and structural reproducibility. Finite element analysis (FEA) is conducted to further elucidate the progressive deformation mechanisms and the optimized stress distribution within this hierarchical structure. Consequently, the engineered sensor achieves an unprecedented balance, delivering high sensitivity (3.779 kPa^{-1}) over a remarkably broad working range (0–255 kPa), alongside a rapid response time (48 ms) and robust durability (over 6000 cycles under a severe load of 150 kPa). Finally, we demonstrate the practical versatility of the sensor through diverse applications, including human physiological monitoring, fruit ripeness discrimination, and backpack carrying-posture assessment, thereby underscoring its immense potential for next-generation human-machine interfaces and intelligent wearable electronics.

2. RESULTS AND DISCUSSION

2.1. Structural Design and Mechanism Analysis of the Multi-layer Flexible Pressure Sensor

Natural load-bearing biological systems often exhibit multilayered heterogeneity, gradient stress distribution, and hierarchical deformation characteristics. These unique features enable efficient force transmission across a broad stress range, providing profound inspiration for the design of high-performance flexible sensing architectures.[31−33] Inspired by these principles, we rationally designed and fabricated a flexible capacitive conical microporous pressure sensor (CMPS). The CMPS features a tri-layer architecture comprising a top TPU electrospun fibrous network, an intermediate layer of SiO_2 micro/nanospheres, and a bottom PDMS/MWCNTs composite substrate patterned with a conical microcavity array. Figure 1a illustrates the 3D exploded schematic of the multi-layered CMPS architecture, accompanied by optical photographs of the macroscopic flexible device and a detailed local cross-sectional view highlighting the structural parameters of the microcavities and the stacked SiO_2 spheres. The fabrication process and further details are provided in Figures S1 and S2. Figure 1b displays the detailed scanning electron microscopy (SEM) and optical microscopy (OM) images characterizing the morphology of each constituent layer. Specifically, the top TPU electrospun fibrous network provides crucial interfacial spatial confinement (Figure 1b(i)), effectively preventing the slippage and detachment of the underlying SiO_2 spheres during cyclic compression. This structural integrity guarantees excellent long-term stability and linear fitting degree of the sensor without sacrificing sensitivity (Figure S3). The intermediate layer consists of multi-size (30 μm/200 nm) SiO_2 spheres randomly stacked on the surface and within the microcavities via spin-coating. This configuration establishes a hierarchical micro/nano-gap structure that facilitates gradient air-gap variations, serving as the core structural basis for the ultrahigh sensitivity observed in the low-pressure regime (Figure 1b(ii)). Meanwhile, the bottom PDMS conical microcavity array functions as the mechanical foundation, providing the essential elastic deformability (Figure 1b(iii)). Fundamentally, the sensing mechanism is governed by the classic capacitance equation:

$$C = \frac{\varepsilon_0 \varepsilon_r A}{d}$$

During compression, the effective dielectric constant (ε_r) increases as the interfacial air is displaced by solid dielectrics, the inter-electrode distance (d) decreases due to structural deformation, and the effective contact area (A) concurrently expands. The synergistic variation of these three parameters drives a significant enhancement in the overall capacitance.

To deeply elucidate the hierarchical capacitive mechanism across diverse pressure regimes, finite element analysis (FEA) and equivalent circuit modeling were performed on a representative structural unit (Figures 1c, S4 and S5). This FEA unit is the most representative structural element of the device, capable of reflecting the overall mechanical properties. Considering that the SiO_2 micro/nanospheres in the actual sample are randomly stacked and have complex contact forms, the modeling process was simplified reasonably. This simplification only affects the local microscopic contact details, slightly influencing the stress distribution in small areas, while the phased deformation characteristics and overall deformation evolution trend of the sensor at the macroscopic level are not affected. Using a single-unit modeling can avoid the result fluctuations and data dispersion caused by the random arrangement of particles, making it convenient to analyze the force transmission and deformation mechanism of hierarchical structures. As

Downloaded from pubs.acs.org/aamick/article-pdf/18/31/43404/6628714/am-2026-09373q.pdf by KOREA UNIV user on 23 September 2026

https://doi.org/10.1021/acsami.6c09373
ACS Appl. Mater. Interfaces 2026, 18, 43404−43417

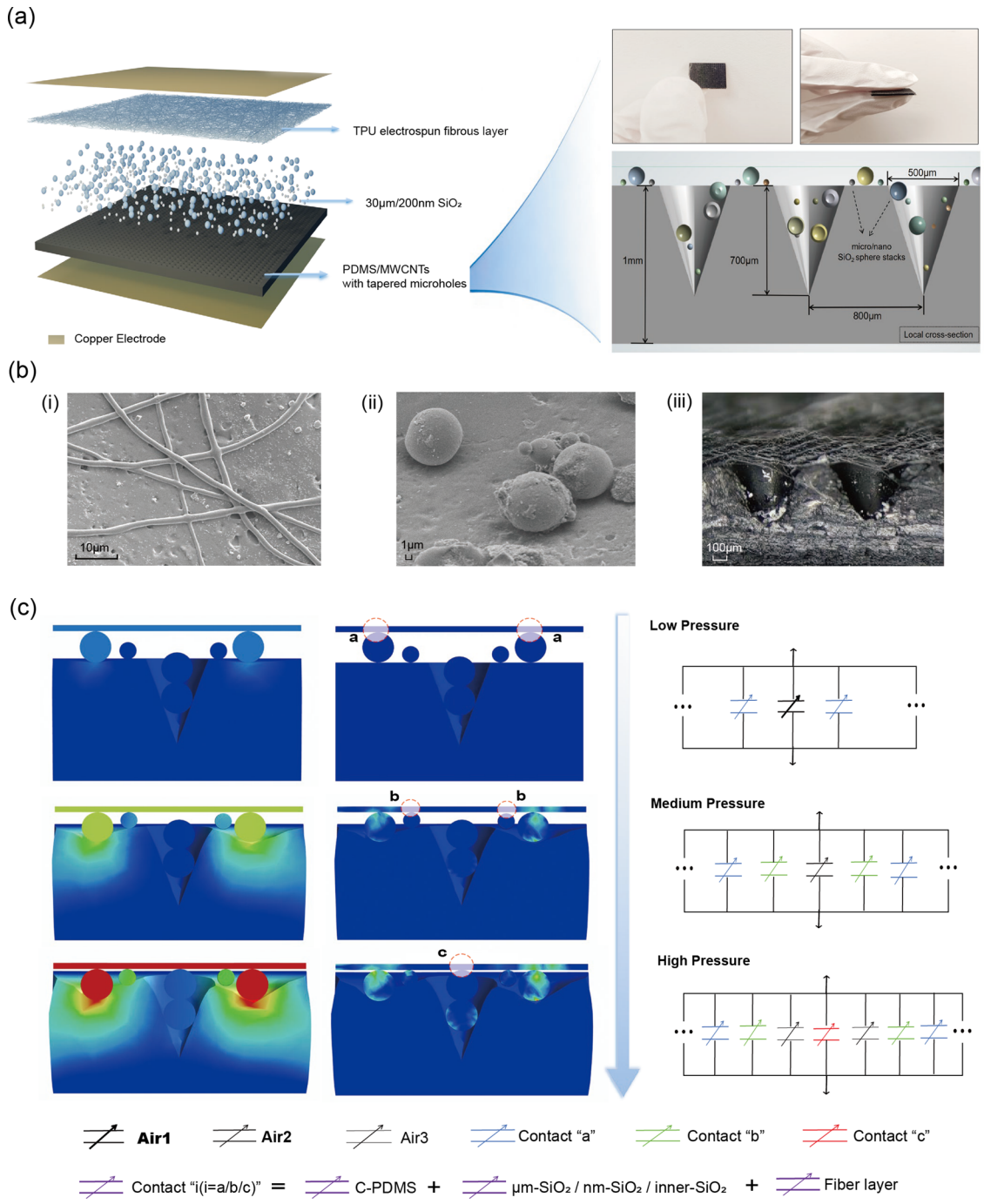


Figure 1. Structural design, morphological characterization, and sensing mechanism of the CMPS. (a) Exploded 3D schematic illustration of the sensor, corresponding optical photographs (top right), and the local cross-sectional schematic highlighting the specific structural dimensions of the conical microcavities (bottom right). (b) Morphological characterizations: (i) TPU electrospun fibers (SEM image), (ii) SiO_2 micro/nanospheres (SEM image), (iii) optical microscopic image of the cross-section of the conical microcavity array (OM image). (c) Finite element analysis (FEA) results of dynamic deformation and stress distribution, as well as equivalent circuit models under low, medium, and high pressure.

shown in Figure 1c, the deformation and stress distribution results of the device under low, medium and high pressure regimes are presented successively. The simulation laws are highly consistent with the capacitance response characteristics measured in subsequent experiments, fully verifying the effectiveness of this modeling scheme. Electrically, the CMPS can be modeled as a dynamic parallel circuit comprising a variable air-gap capacitance (C_{Air}) and a composite solid dielectric capacitance. Specifically, this solid network integrates the capacitive contributions from the PDMS matrix, the multiscale SiO_2 spheres (encompassing micro/nano-scale surface interactions and intra-cavity contacts), and the TPU electrospun layer. In the pristine unloaded state, the fibrous layer remains loose, the spheres are sparsely distributed, and the conical microcavities are entirely undeformed. Consequently, no effective load-transferring contact area is established, yielding a minimal

https://doi.org/10.1021/acsami.6c09373
ACS Appl. Mater. Interfaces 2026, 18, 43404−43417

Downloaded from pubs.acs.org/aamick/article-pdf/18/31/43404/6628714/am-2026-09373q.pdf by KOREA UNIV user on 23 September 2026

baseline capacitance. As the applied pressure escalates, the interfacial contact state of the dielectric layer undergoes a progressive, three-stage structural evolution: (i) Initial Low-Pressure Stage: The highly porous TPU fibrous layer is readily compressed, rapidly expelling inter-fiber air to establish primary effective contacts (denoted as Contact "a") exclusively at the apices of the micro-sized SiO_2 spheres. As this contact area gradually expands, the solid contact unit "a" engages in parallel with the initial air capacitance (C_{Air1}), driving down the overall air proportion. The applied stress is highly concentrated at these local micro-apices, triggering a dramatic initial surge in capacitance and endowing the sensor with an exceptionally high sensitivity. (ii) Medium-Pressure Stage: Upon further loading, the micro-spheres are driven deeper, activating secondary contact interfaces (Contact "b") among the adjacent nano-sized spheres. Concurrently, the underlying PDMS substrate undergoes elastic buckling and compressive deformation, continuously squeezing out residual interfacial air. This synergistic deformation transitions the air capacitance from C_{Air1} to C_{Air2} ($C_{Air1} > C_{Air2}$). The growing proportion of solid dielectrics greatly increases the effective dielectric constant (ε_r), sustaining a stable and robust capacitance response where contact units "a" and "b" operate in parallel with C_{Air2}. (iii) High-Pressure Stage: Under substantial macroscopic compression, the spheres located inside the conical microcavities make contact with the upper interface to form the tertiary contact region (Contact "c"). As this newly densified composite dielectric unit integrates into the circuit, the air capacitance is further minimized to C_{Air3} ($C_{Air2} > C_{Air3}$). At this juncture, the solid dielectric network completely dominates the electrical behavior, causing the capacitance growth rate to gradually decelerate and approach geometric saturation.

2.2. Analysis and Optimization of Sensor Materials and Structure

To evaluate and optimize the performance of the sensor, we conducted tests using an LCR tester, a computer, and a custom compression platform (Figure S6). Initially, the influence of the macroscopic geometric parameters was investigated by varying the conical microcavity diameter (500, 700, and 1000 μm) (Figure S7). As illustrated in Figure 2a, downsizing the cavity diameter from 1000 to 500 μm markedly amplifies the sensitivity. This structural advantage arises from the augmented depth-to-diameter ratio, which simultaneously reduces the equivalent compressive modulus of the dielectric layer and accelerates the interfacial air evacuation rate, thereby facilitating a more rapid variation in the equivalent dielectric constant. Subsequently, the dielectric properties were tailored by adjusting the MWCNT doping concentration within the PDMS matrix (Figure 2b). The incorporation of high-dielectric-constant MWCNTs significantly elevates the sensitivity, achieving an optimal value of 2.54 kPa^{-1} at a 2.5 wt % concentration. However, when the doping concentration is further increased to 2.6 wt %, the continuous conductive pathways gradually form within the dielectric layer due to the doping level approaching the percolation threshold of the composite material, resulting in a significant increase in device leakage current.[34] This leakage current superimposes on the capacitance signal, interfering with the precise measurement by the LCR bridge and causing fluctuations in capacitive response and baseline drift. Meanwhile, the

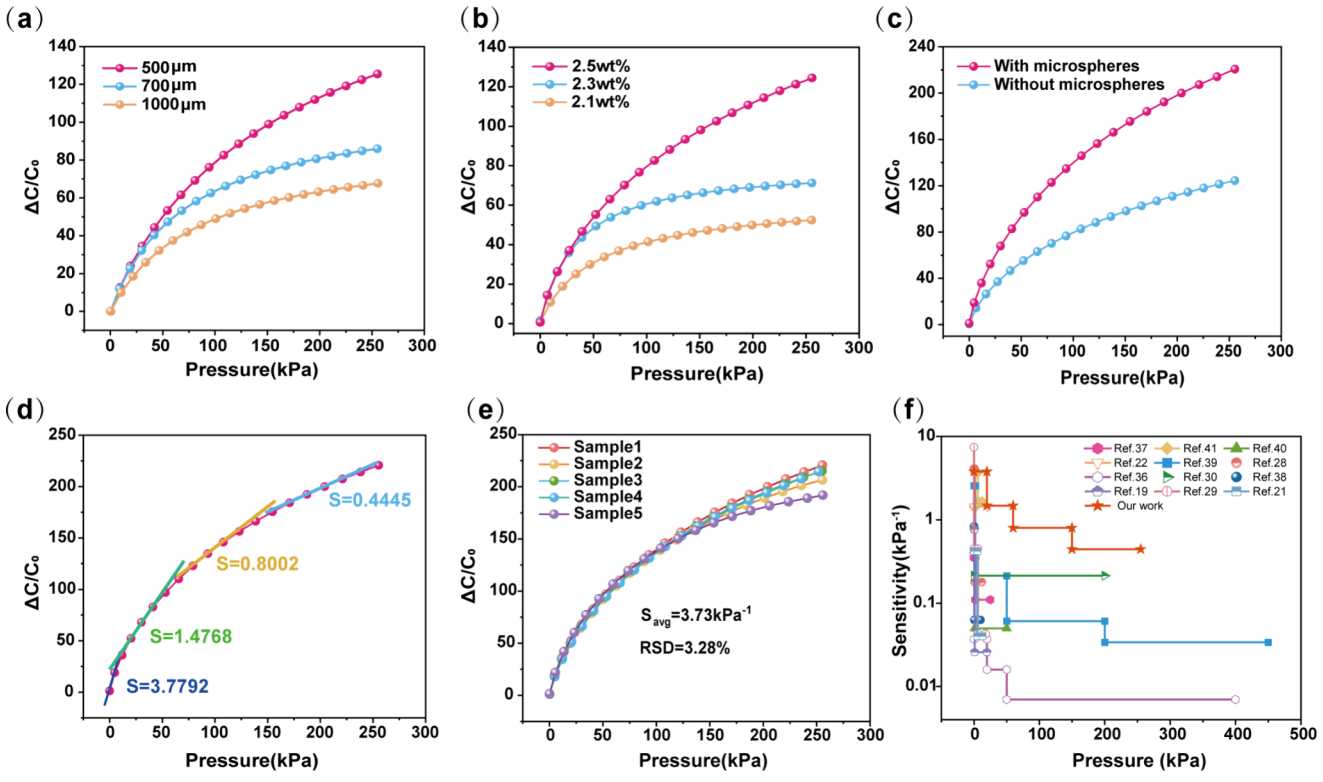


Figure 2. Experimental characterization of CMPS. (a) Comparison of sensor sensitivities for different conical microcavity diameters (500, 700, and 1000 μm). (b) Comparison of sensor sensitivities for different MWCNT contents (2.1, 2.3, and 2.5 wt %). (c) Comparison of sensor sensitivities with and without micro/nano spheres. (d) Capacitance response curve of CMPS. (e) Relative capacitance changes of five independently prepared CMPS. (f) Comparison of sensitivity and measurement range of CMPS with existing studies.

Downloaded from pubs.acs.org/aamick/article-pdf/18/31/43404/6628714/am-2026-09373q.pdf by KOREA UNIV user on 23 September 2026

https://doi.org/10.1021/acsami.6c09373
ACS Appl. Mater. Interfaces 2026, 18, 43404−43417

premature formation of conductive pathways reduces the dynamic tuning range of the dielectric constant under pressure variation, significantly degrading the sensor's sensitivity and stability (Figure S8). Therefore, a doping concentration of 2.5 wt % achieves the optimal balance between enhancing the dielectric constant and maintaining good insulating performance, and is thus identified as the best doping level. Subsequently, multiscale SiO_2 spheres were then incorporated to construct a sophisticated hierarchical architecture. Figure 2c validates that this integration profoundly boosts the overall sensitivity through three synergistic mechanisms: (1) the spheres generate discrete surface protrusions that introduce highly compressible micro-air gaps, prompting sharp dielectric constant variations upon initial loading; (2) the assembled hierarchical microstructures dramatically amplify the rate of change in the effective electrode-dielectric contact area; and (3) their physical incorporation further decreases the overall Young's modulus of the composite.[35] Following this comprehensive multi-parameter optimization, the finalized CMPS demonstrates an exceptionally broad detection range of 0–255 kPa (Figure 2d), featuring a well-defined, step-wise sensitivity profile of 3.77, 1.47, 0.80, and 0.44 kPa^{-1} across the 0–20, 20–60, 60–150, and 150–255 kPa pressure regimes, respectively. Moreover, reliability evaluations across five independently fabricated sensor batches yielded a minimal relative standard deviation of only 3.28% in sensitivity (Figure 2e), confirming superb manufacturing repeatability. Ultimately, as summarized in the comprehensive comparison with recent state-of-the-art studies (Figure 2f and Table S1), our engineered CMPS achieves a superior technological trade-off, simultaneously delivering extraordinary initial sensitivity and an expansive dynamic sensing range.[19,21,22,28−30,36−41]

2.3. Performance Characterization of CMPS

To evaluate the comprehensive sensing performance of the optimized multilayer flexible capacitor pressure sensor, we conducted systematic characterization tests on its key indicators based on the high-precision pressure loading platform mentioned earlier. As illustrated in Figure 3a, the sensor exhibits exceptional dynamic responsiveness. Upon instantaneous light tapping, it achieves rapid response and recovery times of merely 48 and 50 ms, respectively. Furthermore, even under continuous pressing cycles, both metrics remain strictly below 100 ms. These ultra-fast electromechanical rebound characteristics ensure the accurate capture of transient pressure stimuli. Benefiting from the synergistic structural engineering of the multilayer micro/nano composite, the sensor elegantly resolves the typical sensitivity-range trade-off, achieving both ultra-high sensitivity and a broad linear working range. Across a wide pressure sweep from the Pascal regime up to 150 kPa, the device exhibits a stable, step-wise capacitance response (Figure 3b). Notably, it can precisely discriminate a subtle pressure increment of merely 250 Pa in the ultra-low pressure region, underscoring its exceptional cross-scale pressure resolution capabilities. To further validate its dynamic reliability, consecutive cyclic loading-unloading tests were conducted at four representative pressure plateaus (1, 40, 80, and 160 kPa) (Figure 3c). The sensor exhibited highly uniform dynamic responses across the entire pressure spectrum, characterized by stable capacitance amplitudes and negligible baseline drift, thereby confirming its robust cyclic repeatability. Furthermore, to assess the limit of detection for ultra-weak stimuli, lightweight paperclips (~0.2 g) were sequentially stacked onto the sensor surface. Enabled by its superior structural elasticity and high sensitivity, the sensor yields a pronounced and stable step-like capacitance response to these micro-loads with no discernible signal overshoot (Figure 3d). This compellingly verifies its ultra-low limit of detection (LOD) and exceptional resolution for weak mechanical stimuli. Furthermore, the frequency-dependent output characteristics were investigated under a constant pressure of 150 kPa across a frequency sweep from 0.05 to 0.4 Hz (Figure 3e). The highly synchronized waveforms confirm the excellent frequency-independent stability of the sensor. Additionally, the loading-unloading curves (Figure S9) reveal a moderately low mechanical hysteresis of 11.5%. The intrinsic mechanism of low hysteresis and rapid recovery of the device mainly stems from the synergistic effect of hierarchical microstructures: The electrospun TPU fibrous network forms a continuous elastic framework, uniformly dispersing internal strains during loading and coordinating the overall deformation of the composite material to alleviate localized stress concentration and prevent irreversible plastic deformation; after load removal, the TPU's high elasticity fully rebounds, reducing residual deformation-induced hysteresis drift; the multi-size SiO_2 micro/nanospheres construct a large number of adjustable interfacial contact sites, effectively reducing interfacial viscous dissipation, and the particle contact state can be reversibly switched during the loading–unloading process, further inhibiting hysteresis loss. To rigorously evaluate its long-term operational durability, the device was subjected to 6000 continuous loading cycles at an intensive pressure of 150 kPa (Figure 3f). Impressively, the capacitive response exhibited negligible amplitude attenuation throughout the entire process. This superior fatigue resistance is fundamentally attributed to the electrospun fiber layer, which endows the composite architecture with enhanced deformation coordination and mechanical robustness, fully satisfying the stringent requirements for long-term continuous pressure monitoring in practical applications. In practical scenarios such as wearable electronics and dynamic monitoring, flexible sensors are inevitably subjected to repeated bending and twisting. Therefore, we further evaluated the electromechanical stability of the sensor under various bending and twisting states (Figure S10). Considering the unavoidable environmental variations in real-world scenarios, the device's stability was systematically evaluated across a range of temperatures (20–50 °C) and relative humidity levels (40–70% RH) (Figure S11). Remarkably, both factors exerted negligible influence on the sensing performance, demonstrating the exceptional environmental robustness of the sensor.

3. MULTIDIMENSIONAL APPLICATION PROSPECTS OF CMPS

3.1. Motion Posture and Physiological State Monitoring

Driven by rapid response, excellent structural flexibility, and ultra-high sensitivity, the CMPS exhibits tremendous potential for human motion recognition and continuous health monitoring. Interfacing the CMPS with key anatomical sites provides highly reliable quantitative data for biomechanical posture correction and physiological assessment. When mounted on the wrist joint (Figure 4a), the sensor accurately resolves distinct pressure profiles corresponding to varying bending angles, enabling precise kinematic tracking. Attached to the throat

Downloaded from pubs.acs.org/aamick/article-pdf/18/31/43404/6628781/4/am-2026-09373q.pdf by KOREA UNIV user on 23 September 2026

https://doi.org/10.1021/acsami.6c09373
ACS Appl. Mater. Interfaces 2026, 18, 43404−43417

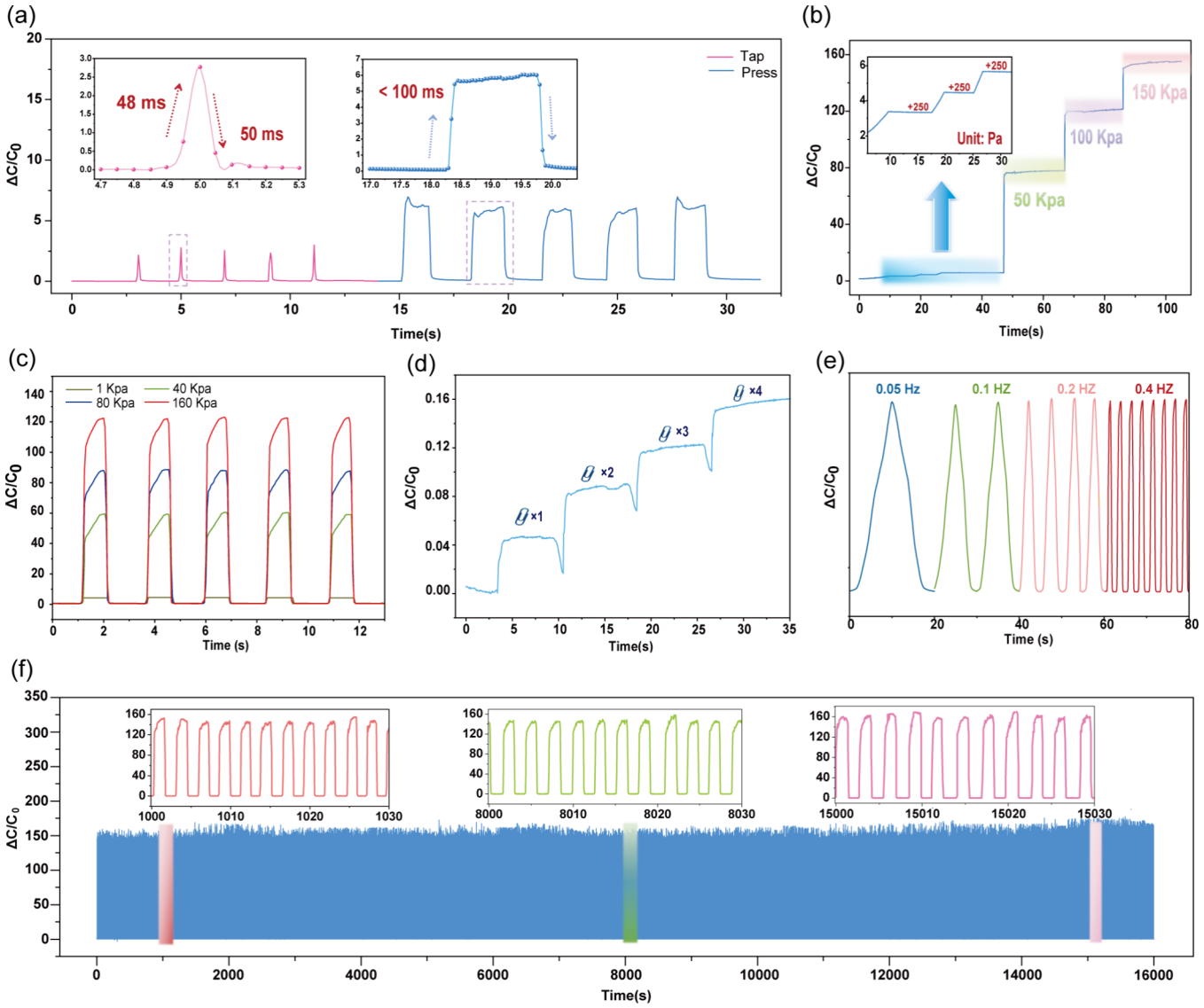


Figure 3. Performance characterization of CMPS. (a) Response/relaxation time of the sensor to light tapping and long pressure. (b) Real-time capacitance change rate of the sensor under step pressure. (c) Normalized capacitance response at 1, 40, 80, and 160 kPa. (d) Step response to an ultra-light object (approximately 200 mg). (e) Relative capacitance changes of the sensor under different vibration frequencies (0.05, 0.1, 0.2, and 0.4 Hz). (f) Durability test of 6000 loading/unloading cycles of the sensor at 150 kPa.

(Figure 4b), the CMPS precisely captures subtle pressure variations induced by swallowing, offering a quantitative metric for assessing deglutition function. Dynamic impact tests on a sensor-integrated knee (Figure 4c) demonstrate robust capabilities in evaluating protective equipment, effectively measuring how a knee pad significantly attenuates peak capacitive amplitude and prolongs buffering duration. Affixed to the cervical spine and wrist (Figure 4d,e), the sensor continuously monitors the neck's forward flexion angle and tennis grip biomechanics, providing real-time feedback on postural deviations to mitigate musculoskeletal injury risks. Beyond physical kinematics, integrating the CMPS inside a face mask (Figure 4f) tracks respiratory patterns to assist in clinical cardiopulmonary function evaluation. Attaching the sensor to the corner of the mouth (Figure 4g) accurately detects micro-muscle contractions during facial expressions, paving the way for diagnostic and rehabilitative monitoring of facial neuropathies like facial palsy.

3.2. Integration into Smart Factory Sorting Systems

Highly sensitive capacitive pressure sensors hold immense promise for automated fruit sorting applications. As illustrated in Figure 5a, modern intelligent production lines utilize robotic arms to sort fruits based on their ripening stages. By integrating the CMPS into mechanical grippers, real-time ripeness evaluation can be successfully achieved. Fruit ripeness is intrinsically linked to its firmness, which dynamically reflects the internal pectin degradation process. Quantifying this mechanical parameter is crucial for accurately assessing the shelf-life of fruits and guiding market distribution. To evaluate the sensor's diagnostic accuracy, the CMPS was mounted onto a robotic gripper configured with a constant indentation depth of 3 mm (Figure 5b) to pick blueberries and cherry tomatoes stored for 1, 3, and 5 days. The measurements reveal that the peak capacitive response decreases significantly with prolonged storage time (Figure 5c,e). This

https://doi.org/10.1021/acsami.6c09373
ACS Appl. Mater. Interfaces 2026, 18, 43404−43417

Downloaded from pubs.acs.org/aamick/article-pdf/18/31/43404/6628781/4/am-2026-09373q.pdf by KOREA UNIV user on 23 September 2026

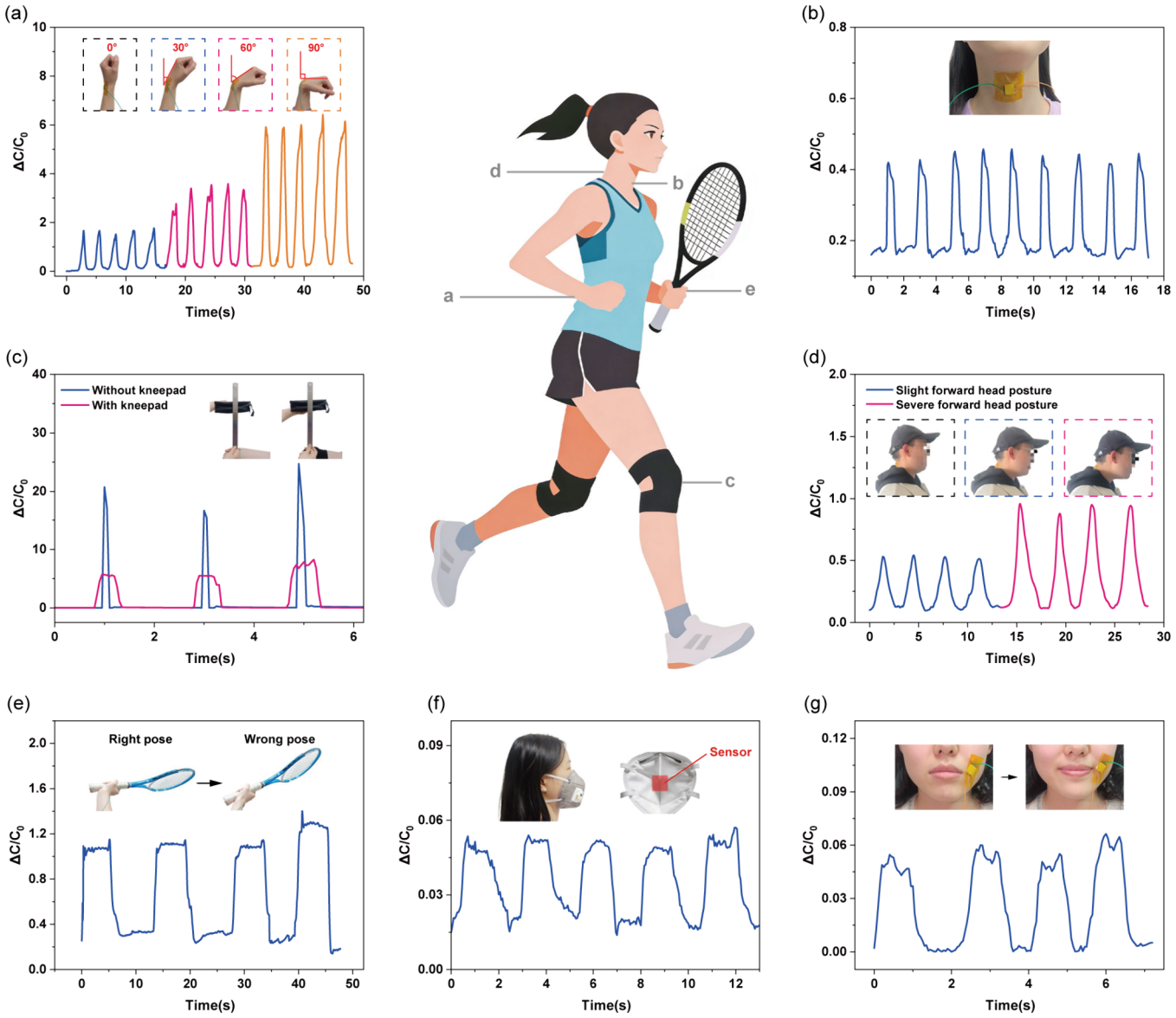


Figure 4. Versatile applications of the CMPS for real-time human kinematics and physiological monitoring. (a) Real-time capacitive responses corresponding to various wrist bending angles (0, 30, 60, and 90°). (b) Detection of swallowing motions by conformally attaching the sensor to the throat. (c) Monitoring of impact forces on the knee joint, comparing scenarios with and without a protective brace. (d) Assessment of cervical posture by detecting different degrees of forward head tilt at the back of the neck. (e) Evaluation of sports biomechanics, differentiating between correct and incorrect tennis gripping postures. (f) Respiratory monitoring capturing dynamic breathing patterns by integrating the sensor inside a face mask. (g) Capacitance response of the sensor at the corner of the mouth to detect facial expression changes.

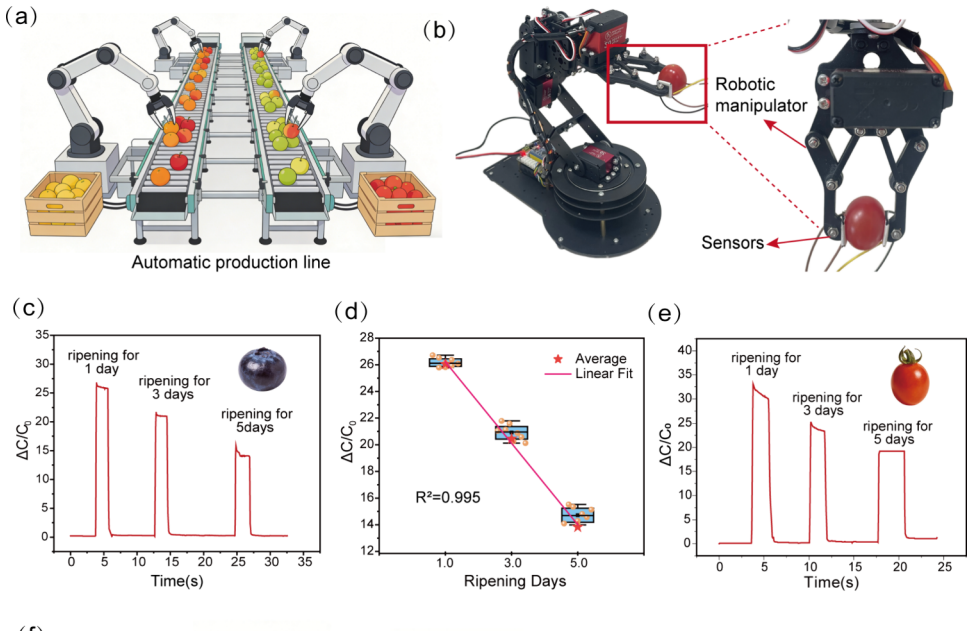
signal attenuation fundamentally stems from pectin degradation and starch hydrolysis during the ripening process, which progressively reduces fruit firmness. Taking blueberries as a representative model, a statistical box plot of the peak capacitance (Figure 5d, 8 per ripening stage) exhibits a robust linear correlation ($R^2 = 0.995$) between storage duration and capacitive output, compellingly validating the feasibility of using CMPS for ripeness discrimination. We further benchmarked the CMPS-based strategy against conventional ripeness assessment techniques (Figure 5f). Traditional visual inspection is straightforward but suffers from subjective bias and a lack of quantitative standards. Biochemical composition analysis boasts high accuracy but relies on destructive sampling, rendering it cumbersome and time-consuming. Machine vision offers a non-contact alternative; however, it incurs high equipment costs and remains highly susceptible to ambient lighting and spatial orientation. Other techniques, such as near-infrared (NIR) spectroscopy and electronic noses, are hindered by exorbitant costs, stringent environmental requirements, or poor long-term stability. In stark contrast, the proposed CMPS-based method strikes an optimal balance among equipment cost, diagnostic accuracy, and detection efficiency. By directly translating subtle firmness variations into distinct capacitive signals, it provides a highly efficient, non-destructive, and real-time solution for industrial-scale fruit sorting.

3.3. Application Demonstration of the CMPS Sensor Array

The growing demand for multidimensional sensing has continuously driven the development of flexible sensor arrays capable

https://doi.org/10.1021/acsami.6c09373
ACS Appl. Mater. Interfaces 2026, 18, 43404−43417

Downloaded from pubs.acs.org/aamick/article-pdf/18/31/43404/6628781/4/am-2026-09373q.pdf by KOREA UNIV user on 23 September 2026



(f)

	Eye observation	Sweetness detection	Image recognition	Our work
Cost	Low	Medium	High	Medium
Precision	Low	High	Medium	Medium
Efficiency	Low	Low	Low	High
Whether Destructive	No	Yes	No	No

Figure 5. Integration of the CMPS for automated fruit ripeness discrimination in smart factory systems. (a) Schematic illustration of an intelligent fruit sorting production line. (b) Photograph of the robotic gripper integrated with the CMPS for non-destructive ripeness evaluation. (c) Dynamic capacitance-time response profiles of blueberries across varying storage durations. (d) Statistical box plot demonstrating the robust correlation between blueberry ripeness (storage time) and peak capacitive response. (e) Capacitance-time response profiles of cherry tomatoes under different storage periods. (f) Comprehensive benchmarking of the proposed CMPS-based strategy against conventional fruit ripeness detection techniques. Panels (a) and (f) were initially generated by AI tools and subsequently modified and recolored by the authors. No other AI tools were used for the remaining panels.

of comprehensively mapping both pressure magnitude and spatial distribution. In this study, a 5 × 3 flexible sensing array was successfully constructed by encapsulating the sensor units with copper foil electrodes and flexible silicone, interconnected via conductive wiring (Figure 6a; specific encapsulation details are provided in Figure S12). To enable the real-time acquisition of dynamic pressure variations across each unit, a custom data acquisition (DAQ) system based on an STM32 microcontroller was specifically designed and implemented (Figure 6b). The corresponding circuit schematics and hardware module functionalities are detailed in Figures S13 and S14. Notably, this highly integrated system autonomously executes signal acquisition and processing, completely eliminating the reliance on bulky external LCR meters and demonstrating superior system-level integration. To evaluate the spatial recognition performance of the fabricated array, 50 g standard weights were sequentially applied to each column to verify the operational integrity and uniform response of all individual channels. Subsequently, a gradient load ranging from 10 to 130 g was applied to the central column, and the corresponding capacitive variations were recorded and translated into a 3D spatial distribution map (Figure 6c). The results vividly demonstrate that the CMPS array can accurately resolve both the precise location and the magnitude of the applied stimuli, exhibiting a strong correlation between the capacitive response and the load mass with remarkably high spatial resolution. These findings fully validate the array's reliability in multipoint pressure identification and quantitative mapping, laying a solid foundation for its future deployment in complex surface tactile sensing and advanced human-machine interaction (HMI) platforms.

3.4. Smart Backpack System for Postural Health Monitoring

Mapping the spatiotemporal distribution of interfacial pressure between backpack straps and human shoulders is crucial for diagnosing musculoskeletal anomalies and preventing postural deformities (e.g., scoliosis and kyphosis). To this end, we integrated two flexible 5 × 3 sensing arrays onto the inner surfaces

https://doi.org/10.1021/acsami.6c09373
ACS Appl. Mater. Interfaces 2026, 18, 43404−43417

Downloaded from pubs.acs.org/aamick/article-pdf/18/31/43404/6628714/am-2026-09373q.pdf by KOREA UNIV user on 23 September 2026

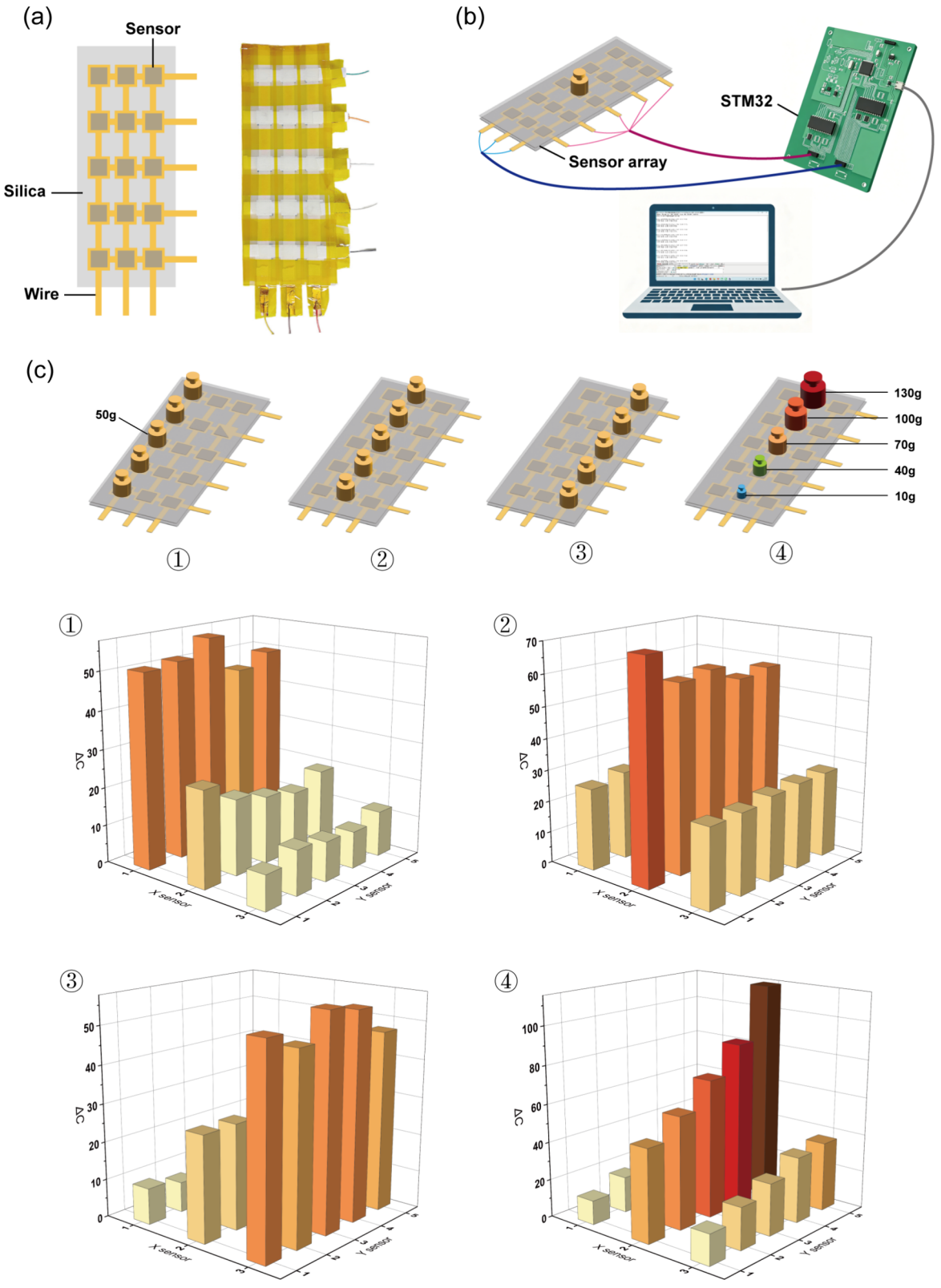


Figure 6. Design and pressure distribution mapping of the CMPS array. (a) Schematic illustration and optical photograph of the 5 × 3 flexible sensing array. (b) Block diagram of the custom data acquisition system based on an STM32 microcontroller. (c) Spatial distribution maps of the array's capacitive response under different applied weights, showing sequential single-column loading and gradient mass loading.

Downloaded from pubs.acs.org/aamick/article-pdf/18/31/43404/6628714/am-2026-09373q.pdf by KOREA UNIV user on 23 September 2026

https://doi.org/10.1021/acsami.6c09373
ACS Appl. Mater. Interfaces 2026, 18, 43404−43417

of a dual-shoulder backpack (Figure S15). Fabricated with a composite architecture of compliant silicone and copper electrodes, the arrays exhibit exceptional mechanical compliance, ensuring conformal adhesion to both the strap and the highly curved human shoulder. Crucially, the sensing coverage effectively encompasses key anatomical landmarks (e.g., the acromion and humeral head) and major muscle groups (e.g., supraspinatus, infraspinatus, and deltoid), thereby guaranteeing comprehensive pressure data acquisition and comfortable wearability during dynamic motion. To facilitate real-time biomechanical assessment, a bespoke data visualization interface was developed to dynamically translate pressure responses into intuitive color-coded heatmaps (Video S1), confirming the system's high sensing fidelity and robust data transmission. Pressure data on both shoulders was recorded under five typical carrying postures: normal backpack, shrugging and hunching, single-shoulder backpacking, uneven shoulder positions, and overly long shoulder straps (Video S2, Figure 7b). Under normal posture (Figure 7c), the pressure distribution on both shoulders remains relatively uniform with the pressure peak concentrated at the acromion, and the overall pressure increases evenly with the load. When carrying a 5 kg load, abnormal postures exhibit distinct pressure distribution characteristics: shrugging and hunching significantly concentrates pressure at the acromion; single-shoulder loading shifts all pressure unevenly to one side; uneven shoulders create significant force disparities; and overly long straps shift the force application downward. Incorrect postures reduce the effective contact area between the shoulder strap and the shoulder, causing significant local pressure concentrations represented as red heat map aggregations. The proposed high-resolution backpack shoulder strap sensing system precisely captures specific pressure abnormalities, and its long-term quantitative monitoring ability provides important references for abnormal posture recognition, intervention, treatment decisions, and rehabilitation evaluation. To further endow the system with intelligent posture recognition, a feedforward neural network (FNN) was constructed to classify the five typical carrying states (Figure 7d). The architecture processes 30 input features (15 channels per shoulder), utilizes two hidden layers (64 and 32 neurons, respectively), combines batch normalization and ReLU activation for feature extraction, and adopts Dropout and L2 regularization to suppress overfitting. Following an 8:2 train-test split, the model underwent forward propagation for posture prediction, employed cross-entropy loss and the Adam optimizer, and updated parameters iteratively via backpropagation. Impressively, the training process demonstrated rapid and stable convergence, along with excellent generalization (Figure 7e), culminating in an exceptional overall classification accuracy of 99.89% on the test set. Furthermore, the precision, recall, and F_1 scores for all posture categories exceeded 99.4% (Table S2), with the confusion matrix confirming the model's robust discriminative power (Figure 7f). This FNN-assisted smart backpack system holds immense promise for diverse health promotion and sports protection applications. For adolescent health, it enables real-time monitoring and early intervention for poor postural habits, providing empirical data for personalized orthopedic treatments. For mountaineers or hikers enduring prolonged heavy loads, real-time pressure feedback can prompt timely posture corrections, mitigating the risk of fatigue-induced compensatory injuries. With its integrated visualization software, this system offers a highly deployable, precision biomechanical tool for campus health screenings, outdoor sports training, and clinical rehabilitation engineering.

4. CONCLUSION

In summary, we have successfully developed a high-performance flexible capacitive pressure sensor featuring a hierarchical architecture, which integrates a dielectric layer of micro-conical arrays, SiO_2 micro/nanospheres, and an electrospun TPU nanofibrous network. Fabricated via a scalable combination of 3D-printed templating, spin coating, and electrospinning, this unique structural synergy fundamentally optimizes stress distribution and dielectric variation. Consequently, the optimized CMPS breaks the conventional trade-off between sensitivity and detection range, achieving an ultrahigh sensitivity of 3.779 kPa^{-1} alongside a remarkably broad sensing range (0–255 kPa). Furthermore, the device exhibits an ultrafast dynamic response (response time $\leq$48 ms) and exceptional mechanical durability (no significant signal degradation after 6000 cycles under a harsh load of 150 kPa). Beyond fundamental characterizations, the CMPS has demonstrated profound versatility in diverse real-world applications. It not only enables precise tracking of human kinematics and physiological signs but also seamlessly integrates into an intelligent robotic arm for automated fruit ripeness evaluation. Crucially, by extending the device into dual 5 × 3 multiplexed arrays embedded within backpack shoulder straps, we realized a deep-learning-assisted wearable system capable of real-time postural monitoring. By simultaneously delivering high sensitivity, a broad dynamic range, and system-level integrability, the proposed sensor architecture paves a highly promising avenue for the next generation of advanced human-machine interfaces, intelligent robotics, and continuous healthcare monitoring.

5. EXPERIMENTAL SECTION

5.1. Preparation of the Dielectric Layer

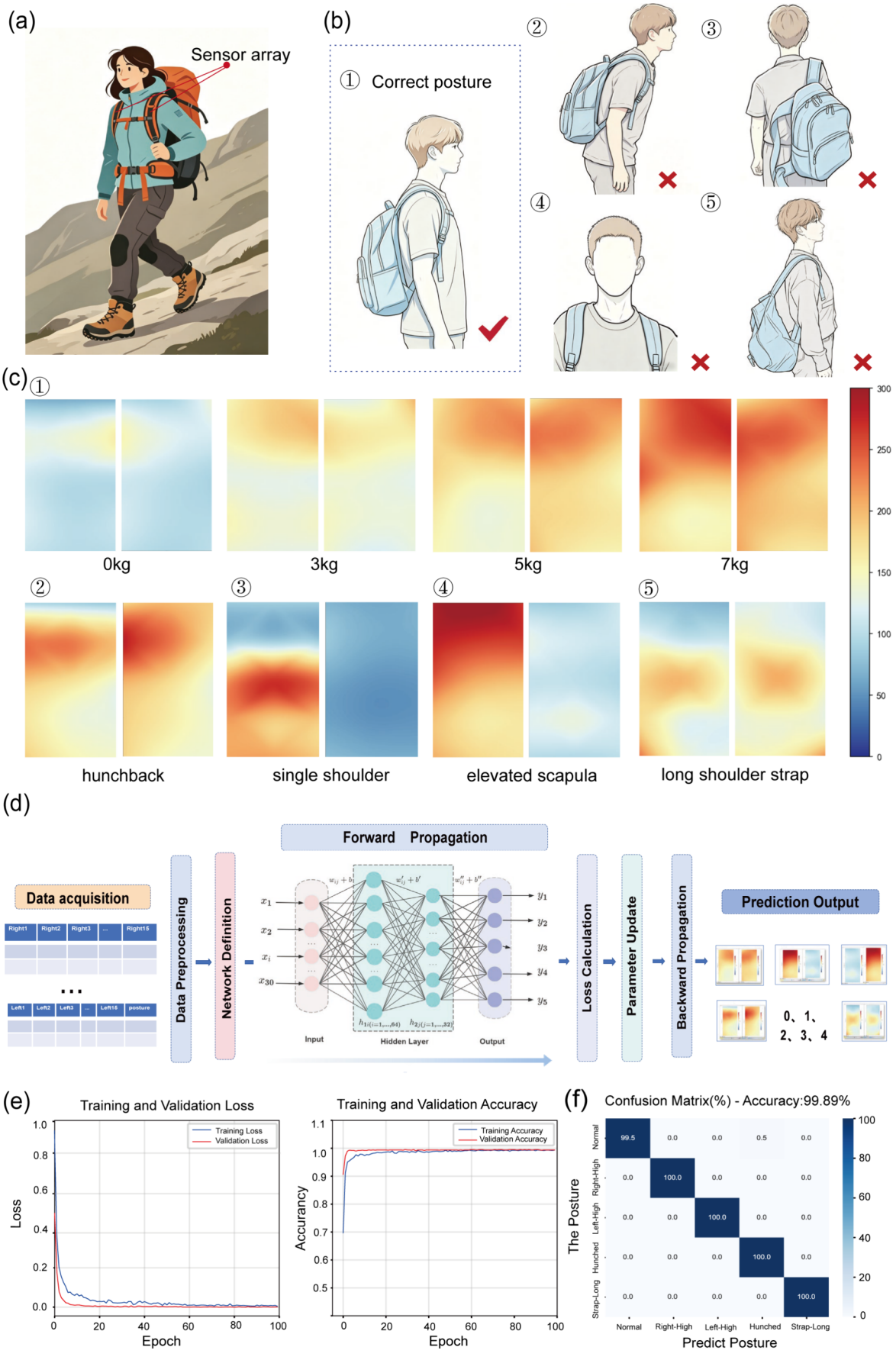
5.1.1. Materials. PDMS and curing agent were purchased from Dow Chemical Silicones Korea Ltd.; MWCNTs were provided by Shenzhen Shuiheng Technology Co., Ltd.; 200 nm silica microspheres were purchased from EPRUI Biotech, Shanghai, China; 30 μm spherical silica and tetrahydrofuran (THF) were purchased from Macklin; N,N-dimethylformamide (DMF) was purchased from Aladdin Biochemical Technology Co., Ltd.

5.1.2. Microstructure C-PDMS Layer. Firstly, a three-dimensional model was designed in Solidworks 2024 and exported as an STL format. The mold was then printed using 3D printing technology. Subsequently, PDMS and curing agent were mixed in a 10:1 weight ratio. A certain proportion of carbon nanotubes (CNTs) was added as needed, and the mixture was placed in a vacuum degassing mixer (1500 rpm, 120 s) to obtain uniformly distributed C-PDMS pre-polymer. The pre-polymer was filled in the mold, and then vacuum degassing (20 min) and thermal curing (80 °C, 8 h) were carried out. The mold was demolded.

5.1.3. SiO_2 Mixed Sphere Layer. 0.1 g of SiO_2 particles with diameters of 30 μm and 200 nm were weighed respectively, and 10 mL of 95 wt % anhydrous ethanol was added for dispersion. The mixture was then vibrated in an ultrasonic instrument for 30 min to form a uniformly dispersed suspension. The C-PDMS sample was placed on a spin-coating instrument, and two different suspensions were coated at low speed of 800 r/min (20 s) and high speed of 1600 r/min (20 s), respectively. Then, it was placed at room temperature to dry (10 min) to allow the ethanol to evaporate, and a mixed particle size SiO_2 layer was formed on the surface.

Downloaded from pubs.acs.org/aamick/article-pdf/18/31/43404/6628781/4/am-2026-09373q.pdf by KOREA UNIV user on 23 September 2026

https://doi.org/10.1021/acsami.6c09373
ACS Appl. Mater. Interfaces 2026, 18, 43404–43417



Downloaded from pubs.acs.org/aamick/article-pdf/18/31/43404/6628714/am-2026-09373q.pdf by KOREA UNIV user on 23 September 2026

https://doi.org/10.1021/acsami.6c09373
ACS Appl. Mater. Interfaces 2026, 18, 43404−43417

Figure 7. continued

Figure 7. Smart backpack system for dynamic shoulder pressure mapping and deep learning-assisted posture recognition. (a) Schematic illustration of the wearable monitoring scenario using the sensor-integrated backpack. (b) Photographs depicting the five typical carrying postures: normal, shrugging/kyphosis, unilateral carrying, asymmetrical shoulders, and loose straps. (c) Corresponding spatiotemporal heatmaps of bilateral shoulder pressure distribution under incremental loads (0, 3, 5, and 7 kg) in the normal state, and under various anomalous postures at a 5 kg load. (d) Architecture and data processing workflow of the feedforward neural network (FNN) employed for intelligent posture classification. (e) Evolution curves of the loss function and classification accuracy during the model training and validation phases. (f) Confusion matrix of the trained FNN model, demonstrating an overall classification accuracy of 99.89%. The initial lines and contours of panel (a) were generated using AI-assisted tools. The authors subsequently performed all editing, coloring, and final modifications.

5.1.4. TPU Electrospinning Layer. Firstly, 5 mL of DMF and THF were measured, 13 wt % TPU (1.3696 g) was added, and magnetic stirring (60 °C, 4 h) was performed to completely dissolve. Then, the TPU was electrospun onto the aforementioned dielectric layer surface. During the entire process, the receiving distance was maintained at a constant 15 cm, the negative voltage was set at 2.1 kV, and the positive voltage was adjusted to approximately 8.1 kV based on the actual filament output status to ensure continuous and stable filament output. The spinning time was limited to 10–20 s to achieve the required thin layer thickness.

5.2. Characterization and Performance Testing

The multi-layer dielectric layer microstructure morphology was characterized using an electron microscope. Five parallel samples were prepared to ensure testing reliability. The sensor was compressed loaded using a universal testing machine (ESM303, Mark-10) and tested in real time at 100 kHz with an LCR digital bridge (TH2829C, Tonghui Electronics).

5.3. Finite Element Simulation

Static finite element simulation was conducted using Ansys Mechanical 2024 R2 software to analyze the contact deformation evolution law under different pressure intervals. Considering that the SiO_2 microspheres in the actual preparation were in a random stacking state, a proportional enlarged single-cone-shaped micro-hole element model was used to illustrate the mechanism. Automatic meshing was adopted, and the calculation grid was constructed with second-order tetrahedral elements (Tet10), with a minimum element edge length of 0.5 mm, generating 2580 elements and 6182 nodes. The bottom surface of the model was subjected to fixed support constraints, and the top surface was subjected to a force load. The compression condition was simulated.

5.4. Development of the Test System

A dedicated signal acquisition PCB system was developed based on STM32. The core control unit was the STM32F103 series microcontroller, and the onboard CH340 chip was used to achieve USB-TTL serial communication. Two 74LS154 encoders were used to expand the channels. In summary, the hardware system specifically includes a 5 × 3 array capacitance sensor module, a row and column selection module, a signal measurement circuit, a microcontroller module, and a power management module. During testing, the X1–X5 and Y1–Y3 channels of the sensor were connected to the corresponding acquisition ports. The data line was connected to the upper computer, and the CH340 driver was installed. The baud rate and port number were set, and the real-time capacitance data of the sensor could be collected, transmitted, and recorded through the serial port.

5.5. Implementation Process of the Visualization Function

In the double-shoulder-belt response data visualization, the host-side Python program receives the raw data transmitted by the window. Firstly, it calls the griddate function from the SciPy library to perform cubic interpolation upsampling on the 5 × 3 array data, converting the discrete measurement point data into a continuous distribution image with a resolution of 100 × 60. Then, it uses the imshow function from the Matplotlib library and the RdYlBu_r color mapping (blue, yellow, red) to generate a dynamic heat map, with the update frequency synchronized with the data sampling rate to ensure real-time reflection of data change characteristics.

5.6. Dataset Construction for Deep Learning

This test involves 4 participants, covering different heights (158–172 cm) and weights (40–80 kg). The test subjects perform 5 postures (normal, right shoulder high, left shoulder high, shrugging and hunching, long shoulder straps), and each posture is tested with 4 loads (0, 3, 5, and 7 kg), each lasting 20–30 s. Real-time data of both shoulder straps is collected. After screening, 4624 sets of data are retained as the original database. Additionally, to enhance the robustness and anti-interference performance of the model in practical scenarios, Gaussian perturbations are introduced within a reasonable signal standard deviation range (<5%) in the standardized training data to strengthen the model's tolerance to minor fluctuations. Gaussian perturbation serves as a data-level regularization technique. The introduced stochastic noise enables implicit sample augmentation and decision boundary smoothing, which limits model complexity, facilitates the extraction of generalizable features, and suppresses overfitting under small-sample conditions.

■ ASSOCIATED CONTENT

Supporting Information

The Supporting Information is available free of charge at https://pubs.acs.org/doi/10.1021/acsami.6c09373.

(a) Fabrication of dielectric layer with conical microcavity structure: (i) PDMS, curing agent, and MWCNTs were mixed thoroughly in a plastic bottle; (ii) the mixture was poured into a resin mold and cured; (iii) the dielectric layer was obtained after demolding, (b) Introduction of SiO_2 microspheres: (i) SiO_2 microspheres were dispersed with ethanol to form a suspension; (ii) the suspension was spin-coated onto the dielectric layer; (iii) after drying, a dielectric layer coated with SiO_2 microspheres was obtained, (c) Preparation of the TPU spinning layer: (i) TPU was added into a mixed solvent of DMF and THF, followed by heating and stirring to form a homogeneous solution; (ii) electrospinning was performed; (iii) the final TPU spinning layer was obtained (Figure S1); (a) Top-view of the dielectric layer with conical microcavity structure, (b) cross-sectional view of the dielectric layer, (c) top view of the dielectric layer after introducing SiO_2 microspheres and the TPU spinning layer, (d) cross-sectional view of the dielectric layer after introducing SiO_2 microspheres and the TPU spinning layer (Figure S2); Comparison of sensor performance before and after the introduction of the TPU spinning layer (Figure S3);

Downloaded from pubs.acs.org/aamick/article-pdf/18/31/43404/6628/7814/iam-2026-09373q.pdf by KOREA UNIV user on 23 September 2026

https://doi.org/10.1021/acsami.6c09373
ACS Appl. Mater. Interfaces 2026, 18, 43404–43417

Finite element regular mesh division detail diagram: 3D view and 2D cross-section (Figure S4); Finite element analysis results of CMPS at three contact states: von Mises equivalent stress distribution (upper, unit: Pa) and deformation nephograms (lower) (Figure S5); (a) Electromechanical compression stage, (b) LCR meter, (c) Control/DAQ computer (Figure S6); Samples with different conical pore diameters: from left to right, 500, 700, and 1000 μm (Figure S7); Performance Curve of CMPS (2.6 wt %) (Figure S8); Performance comparison of flexible capacitive pressure sensors in recent articles (Table S1); Capacitive response curves of pressure sensor under cyclic loading at 70 kPa (Figure S9); (a) Bending, (b) Twisting (Figure S10); (a) Humidity effect, (b) Temperature effect (Figure S11); (a) Vertical electrode surface, (b) Transverse electrode surface (Figure S12); Circuit Schematic Diagram of Sensor Array Wiring (Figure S13); The physical prototype of the circuit board and the functions of each part (Figure S14); Two sensor arrays are fixed inside the inner side of the backpack shoulder strap (Figure S15); Classification performance metrics of the proposed model on the test set (Table S2) (DOCX)

Movie S1: The color changes in the shoulder strap pressure heatmap caused by applying pressure to different positions of the sensor array (MP4)

Movie S2: Demonstration of the real-time changes in pressure under different backpack postures (MP4)

AUTHOR INFORMATION

Corresponding Author

Zhi-Jun Zhao – *Institute of Smart City and Intelligent Transportation, Southwest Jiaotong University, Chengdu 611756, China;* orcid.org/0000-0002-4981-5062; Email: zhaozhijun@swjtu.edu.cn

Authors

Jiaqi Xu – *Institute of Smart City and Intelligent Transportation, Southwest Jiaotong University, Chengdu 611756, China*

Lanxin Ji – *Institute of Smart City and Intelligent Transportation, Southwest Jiaotong University, Chengdu 611756, China*

Peizhi Jiang – *Institute of Smart City and Intelligent Transportation, Southwest Jiaotong University, Chengdu 611756, China*

Jiawei Wu – *Southwest Jiaotong University-Leeds Joint School, Chengdu 611756, China*

Yun-Woo Lee – *Department of Mechanical Engineering, Soongsil University, 369 Sangdo-ro, Dongjak-Gu, Seoul 06978, Korea*

Junseong Ahn – *Department of Control and Instrumentation Engineering, Korea University, Sejong 30019, Republic of Korea;* orcid.org/0000-0002-4090-5440

Bingjun Yu – *Tribology Research Institute, School of Mechanical Engineering, Southwest Jiaotong University, Chengdu 610031, China;* orcid.org/0000-0002-8281-1899

Caijiang Lu – *Tribology Research Institute, School of Mechanical Engineering, Southwest Jiaotong University, Chengdu 610031, China*

Complete contact information is available at: https://pubs.acs.org/doi/10.1021/acsami.6c09373

Author Contributions

‡J.X., L.J. and P.J. contributed equally to this study. They jointly conceived the new hypotheses, conducted all experimental work, performed data integration and analytical interpretation, and drafted the initial manuscript. They performed computational modeling through finite element analysis and constructed the test circuitry. L.J. and J.W. developed the deep learning architectures. Y.-W.L., J.A., B.Y., C.L. and Z.-J.Z. provided critical academic guidance and oversaw the project's overall direction.

Notes

The authors declare no competing financial interest.

ACKNOWLEDGMENTS

This work was supported by the National Natural Science Foundation of China (no. 52375578), in part by the Fundamental Research Funds for the Central Universities (2682025CG001).

REFERENCES

(1) Yu, G.; Zhang, Q.; Wang, M.; Lu, H.; Chen, Z.; Liu, J.; Chen, C.; Wang, S.; Ma, Y.; Yue, Y. Osmotic Energy Directly Driving Flexible All-Solid-State 2D Nanofluidic Pressure Sensors. *Adv. Mater.* **2025**, *37*, e06990.

(2) Wu, X.; Liang, Y.; Lu, L.; Yang, S.; Liang, Z.; Liu, F.; Lu, X.; Xiao, B.; Zhong, Y.; Xie, Y. Fabric-Based Flexible Pressure Sensor Arrays with Ultra-Wide Pressure Range for Lower Limb Motion Capture System. *Research* **2025**, *8*, 0835.

(3) Guo, X.; Zhu, X.; Long, Q.; Wu, X.; Li, Z.; Li, J.; Zhang, T.; Qian, X.; Li, X.; Chen, Y.; Zhu, S.; Hong, W.; Hong, Q.; Zhao, Y. Multifunctional pressure and humidity sensor modulated by electrostatic interactions and hydrogen bonds for wearable health monitoring. *J. Colloid Interface Sci.* **2025**, *678*, 1061.

(4) Liu, Y.; Zhang, L.; Wang, H.; Li, Y.; Zhao, J. Multifunctional Conductive Hydrogel-Based Flexible Pressure Sensor with Ultrahigh Sensitivity and Wide Linear Range. *ACS Appl. Mater. Interfaces* **2025**, *17*, 34562–34571.

(5) Feng, B.; Li, W. J.; Cui, Z.; Li, Y.; He, W.; et al. ITO Nanoparticles to Stabilize the Self-Assembly of Hole Transport Layer in Inverted Perovskite Solar Cells. *Adv. Mater.* **2026**, *38*, 2517426.

(6) Xu, C.; Chen, J.; Zhu, Z.; Liu, M.; Lan, R.; Chen, X.; Tang, W.; Zhang, Y.; Li, H. Flexible Pressure Sensors in Human–Machine Interface Applications. *Small* **2023**, *20*, 2306655.

(7) Mathew, S.; Vandrangi, S. K.; Chintagumpala, K. Smart Sensing with PDMS-Bi_2O_3 Composites: A Flexible Capacitance Pressure Sensor for Wearables and Voice Interfaces. *Sens. Actuators A Phys.* **2026**, *405*, 117833.

(8) Yan, X.; Li, Y.; Zhang, Y.; Bai, W.; Kou, H. High Sensitivity Iontronic Flexible Pressure Sensor Based on Microstructured Electrodes for Wearable Devices. *IEEE Instrum. Meas. Mag.* **2026**, *29*, 4–11.

(9) Kim, S. W.; Lee, J. H.; Ko, H. J.; Lee, S.; Bae, G. Y.; Kim, D.; Lee, G.; Lee, S. G.; Cho, K. Mechanically Robust and Linearly Sensitive Soft Piezoresistive Pressure Sensor for a Wearable Human-Robot Interaction System. *ACS Nano* **2024**, *18* (4), 3151–3160.

(10) Zhang, T.; Zhao, Y.; Long, Q.; Zhu, X.; He, L.; Li, Z.; Qian, X.; He, X.; Li, J.; Lv, C.; Zha, Y.; Chen, Y.; Hong, W.; Hong, Q.; Guo, X. Graphene/MXene/Cellulose cellulosic paper-based flexible bifunctional sensors utilizing molecular bridge strategy with tunable

Downloaded from pubs.acs.org/aamick/article-pdf/18/31/43404/6628714/am-2026-09373q.pdf by KOREA UNIV user on 23 September 2026

piezoresistive effect for Temperature-Pressure sensing. *Chem. Eng. J.* **2024**, *498*, 154972.
(11) Luo, J. Q.; Zhang, L. B.; Wu, T.; Song, H. J.; Tang, C. L. Flexible Piezoelectric Pressure Sensor with High Sensitivity for Electronic Skin Using Near-Field Electrohydrodynamic Direct-Writing Method. *Extreme Mech. Lett.* **2021**, *48*, 101279.
(12) Yang, Y.; Pan, H.; Xie, G. Z.; Jiang, Y. D.; Chen, C. X.; Su, Y. J.; Wang, Y.; Tai, H. L. Flexible Piezoelectric Pressure Sensor Based on Polydopamine-Modified $BaTiO_3$/PVDF Composite Film for Human Motion Monitoring. *Sens. Actuators A: Phys.* **2020**, *301*, 111789.
(13) Chamankar, N.; Khajavi, R.; Yousefi, A. A.; Rashidi, A.; Golestanifard, F. A Flexible Piezoelectric Pressure Sensor Based on PVDF Nanocomposite Fibers Doped with PZT Particles for Energy Harvesting Applications. *Ceram. Int.* **2020**, *46* (12), 19669–19681.
(14) Xia, K. Q.; Yang, S.; Lu, J. G.; Yu, M. Intrinsic Static-Dynamic Triboelectric Pressure Sensor Enabled by Charge Excitation and 3D Gradient Engineering for Intelligent Dual-Mode Control. *Chem. Eng. J.* **2025**, *525*, 170270.
(15) Zhong, Y.; Wang, J. Q.; Han, L.; Dai, S. P.; Zhu, H.; Hua, J.; Cheng, G. G.; Ding, J. N. High-Performance Flexible Self-Powered Triboelectric Pressure Sensor Based on Chemically Modified Micropatterned PDMS Film. *Sens. Actuators A: Phys.* **2023**, *349*, 114013.
(16) Cui, C.; Qin, Y.; Zeng, Y.; Lu, X.; Wei, E.; Xie, J. A flexible capacitive pressure sensor with dual-layer microstructure for health monitoring. *Sens. Actuators A: Phys.* **2024**, *377*, 115709.
(17) Wang, H. Z.; Li, Z.; Liu, Z. Y.; Fu, J. K.; Shan, T. Y.; Yang, X. Y.; Lei, Q. Y.; Yang, Y. J.; Li, D. H. Flexible Capacitive Pressure Sensors for Wearable Electronics. *J. Mater. Chem. C* **2022**, *10* (5), 1594–1605.
(18) Zeng, Y.; Qin, Y. F.; Yang, Y. P.; Lu, X. Y. A Low-Cost Flexible Capacitive Pressure Sensor for Health Detection. *IEEE Sens. J.* **2022**, *22* (8), 7665–7673.
(19) Lv, L. Y.; Liu, T. X.; Jiang, T.; Li, J. M.; Zhang, J.; Zhou, Q. H.; Dhakal, R.; Li, X.; Li, Y. Y.; Yao, Z. A Highly Sensitive Flexible Capacitive Pressure Sensor with Hierarchical Pyramid Micro-Structured PDMS-Based Dielectric Layer for Health Monitoring. *Front. Bioeng. Biotechnol.* **2023**, *11*, 1303142.
(20) Huang, L. S.; Huang, X.; Zhang, P.; Li, Y. X.; Wang, S.; Bu, X. F.; Chen, Z. F. Flexible Capacitive Pressure Sensor with Synergistic Effect Between Double-Sided Pyramid Sponge Structure Dielectric Layer and Fiber Structure Electrode Layer. *Sens. Actuators A: Phys.* **2024**, *369*, 115153.
(21) Luo, Y. S.; Shao, J. Y.; Chen, S. R.; Chen, X. L.; Tian, H. M.; Li, X. M.; Wang, L.; Wang, D. R.; Lu, B. H. Flexible Capacitive Pressure Sensor Enhanced by Tilted Micropillar Arrays. *ACS Appl. Mater. Interfaces* **2019**, *11* (19), 17796–17803.
(22) Lv, C.; Tian, C.; Jiang, J.; Dang, Y.; Liu, Y.; Duan, X.; Li, Q.; Chen, X.; Xie, M. Ultrasensitive Linear Capacitive Pressure Sensor with Wrinkled Microstructures for Tactile Perception. *Adv. Sci.* **2023**, *10* (14), 2206807.
(23) Yang, J.; Chen, X.; Zhang, Y.; Wei, Q.; Lee, S. G.; Zhu, Y. Surface Wrinkling for Flexible and Stretchable Sensors. *Small* **2022**, *18* (36), 2203491.
(24) Lin, Z.; Pan, Z.; Qin, B.; Kong, H.; Ye, S.; Wu, H.; Bian, C.; Shen, G.; Chen, Y.; Zhang, C. Bioinspired Iontronic Pressure Sensor with Ultrawide Range and High Sensitivity. *ACS Sens.* **2025**, *10* (9), 6991–7001.
(25) Wang, J.; Jia, X.; Yu, D.; Yao, L.; Jia, Y. One-Step Molded Free-Standing Liquid Metal Electrode and Its Application in Wearable Pressure Sensors. *ACS Appl. Nano Mater.* **2025**, *8* (8), 4067–4076.
(26) Yang, W.; Ding, W.; Liu, M.; Yang, J.; Li, M. A theoretical model of a flexible capacitive pressure sensor with microstructured electrodes for highly sensitive electronic skin. *J. Phys. D: Appl. Phys.* **2022**, *55* (9), 094001.
(27) Zhang, P.; Zhang, J.; Li, Y. X.; Huang, L. S. Flexible and high sensitive capacitive pressure sensor with microstructured electrode inspired by ginkgo leaf. *J. Phys. D: Appl. Phys.* **2021**, *54* (46), 465401.
(28) Li, S.; Wang, Y.; Wu, Y.; Asghar, W.; Xia, X.; Liu, C.; Bai, X.; Shang, J.; Liu, Y.; Li, R.-W. Piezo-Capacitive Flexible Pressure Sensor with Magnetically Self-Assembled Microneedle Array. *ACS Sens.* **2025**, *10* (2), 1063–1071.
(29) Li, H. Y.; Zhang, C. J.; Xu, H. Y.; Yang, Q.; Luo, Z. X.; Li, C.; Kai, L.; Meng, Y. Z.; Zhang, J. L.; Liang, J. Microstructured Liquid Metal-Based Embedded-Type Sensor Array for Curved Pressure Mapping. *Adv. Sci.* **2025**, *12* (3), 2413233.
(30) Zhong, Y.; Liu, K.; Wu, L.; Ji, W.; Cheng, G.; Ding, J. Flexible Tactile Sensors with Gradient Conformal Dome Structures. *ACS Appl. Mater. Interfaces* **2024**, *16* (39), 52966–52976.
(31) Tang, X.; Wu, C.; Gan, L.; Zhang, T.; Zhou, T.; Huang, J.; Wang, H.; Xie, C.; Zeng, D. Multilevel Microstructured Flexible Pressure Sensors with Ultrahgh Sensitivity and Ultrawide Pressure Range for Versatile Electronic Skins. *Small* **2019**, *15*, 1804559.
(32) Mahata, C.; Algadi, H.; Lee, J.; Kim, S.; Lee, T. Biomimetic-inspired micro-nano hierarchical structures for capacitive pressure sensor applications. *Measurement* **2020**, *151*, 107095.
(33) Qin, Y.; Wang, X.; Gao, B. Ionic Capacitive Pressure Sensor with Enhanced Sensitivity and Broad Detection Range Featuring Hierarchical Microridge Design. *ACS Appl. Electron. Mater.* **2025**, *7* (6), 2494–2503.
(34) Elaskalany, M.; Behdinan, K. Effect of Carbon Nanotube Type and Length on the Electrical Conductivity of Carbon Nanotube Polymer Nanocomposites. *Mater. Res. Express* **2023**, *10* (10), 105010.
(35) Zhou, Y.; Wang, Y.; Li, G.; Xuan, S.; Zeng, Q.; Guo, Y.; Luo, Y.; Feng, D. Fast-Response and Flexible Triboelectric Pressure Sensors with Hierarchical Triple-Scale Structure for Wireless Smart Seat Detection. *Small* **2025**, *21* (48), e09357.
(36) Wei, W.; Wang, J.; Zhang, X.; Luo, X.; Chen, B.; Shen, X.; Yuan, L.; Huang, Y.; Long, Y. 3D Printing for Capacitive Flexible Pressure Sensors of Small Pressure High Sensitivity with Microdome-Labyrinth Structure. *Smart Mater. Struct.* **2025**, *34* (1), 015012.
(37) Guo, Y.; Gao, S.; Yue, W.; Zhang, C.; Li, Y. Anodized Aluminum Oxide-Assisted Low-Cost Flexible Capacitive Pressure Sensors Based on Double-Sided Nanopillars by a Facile Fabrication Method. *ACS Appl. Mater. Interfaces* **2019**, *11* (51), 48594–48603.
(38) Shi, R. L.; Lou, Z.; Chen, S.; Shen, G. Z. Flexible and Transparent Capacitive Pressure Sensor with Patterned Microstructured Composite Rubber Dielectric for Wearable Touch Keyboard Application. *Sci. China Mater.* **2018**, *61* (12), 1587–1595.
(39) Shang, E.; Zhao, Z.; Peng, S.; Zhang, N.; Fan, D.; Liu, Y. Flexible Linkage Design of Composite Dielectric Layer for High-Performance Capacitive Pressure Sensor. *ACS Appl. Electron. Mater.* **2025**, *7* (11), 5050–5060.
(40) Luo, Z.; Chen, J.; Zhu, Z.; Li, L.; Su, Y.; Tang, W.; Omisore, O. M.; Wang, L.; Li, H. High-Resolution and High-Sensitivity Flexible Capacitive Pressure Sensors Enhanced by a Transferable Electrode Array and a Micropillar–PVDF Film. *ACS Appl. Mater. Interfaces* **2021**, *13* (6), 7635–7649.
(41) Kurup, L. A.; Arthur, J. N.; Yambem, S. D. Highly Sensitive Capacitive Low-Pressure Graphene Porous Foam Sensors. *ACS Appl. Electron. Mater.* **2022**, *4* (8), 3962–3972.

Downloaded from pubs.acs.org/aamick/article-pdf/18/31/43404/6628714/am-2026-09373q.pdf by KOREA UNIV user on 23 September 2026

https://doi.org/10.1021/acsami.6c09373
ACS Appl. Mater. Interfaces 2026, 18, 43404–43417